AGU100 ADVANCING EARTH AND SPACE SCIENCE

Geophysical Research Letters

RESEARCH LETTER
10.1002/2018GL077409

Special Section:
New understanding of the solar eclipse effects on geospace: The 21 August 2017 Solar Eclipse

Key Points:
- Model-data comparisons showed a relatively consistent depletion and enhancement in the ionosphere during and after the eclipse
- GITM showed that the divergence of horizontal winds drove the increased O after the eclipse allowing an increase in the ionization rate
- Slower charge exchange due to both the decreased ion temperature and N_2 density allowed an increase of O^+ density in the *F* region also

Supporting Information:
- Supporting Information S1

Correspondence to:
A. J. Ridley,
ridley@umich.edu

Citation:
Wu, C., Ridley, A. J., Goncharenko, L., & Chen, G. (2018). GITM-data comparisons of the depletion and enhancement during the 2017 solar eclipse. *Geophysical Research Letters*, *45*, 3319–3327. https://doi.org/10.1002/2018GL077409

Received 31 JAN 2018
Accepted 22 MAR 2018
Accepted article online 30 MAR 2018
Published online 16 APR 2018

GITM-Data Comparisons of the Depletion and Enhancement During the 2017 Solar Eclipse

Chen Wu[1,2], A. J. Ridley[2], Larisa Goncharenko[3], and Gang Chen[1]

[1]Electronic Information School, Wuhan University, Wuhan, China, [2]Climate and Space Sciences and Engineering, University of Michigan, Ann Arbor, MI, USA, [3]Haystack Observatory, Massachusetts Institute of Technology, Westford, MA, USA

Abstract The total solar eclipse of 21 August 2017 was simulated with the Global Ionosphere-Thermosphere Model (GITM), and the results were compared with the total electron content (TEC) measurements provided by the Global Navigation Satellite System, as well as F2 layer peak electron density (NmF2) derived from six ionosondes. TEC decreased over North America by ~54.3% in the model and ~57.6% in measurements, and NmF2 decreased by ~20–50% in the model and ~40–60% in the measurements. GITM predicted a posteclipse enhancement of ~10% in TEC and NmF2, consistent with observations which suggested an increase of ~10–25% in TEC and ~10–40% in NmF2. GITM showed that the divergence of horizontal winds drove the increase in Oxygen after the eclipse allowing an increase in the ionization rate. The slower charge exchange due to both the decreased ion temperature and N_2 density allowed an increase of O^+ density in the *F* region also.

Plain Language Summary The total solar eclipse of 21 August 2017 was explored with the Global Ionosphere-Thermosphere Model, which simulates weather in space. The results were compared with ionospheric observations from the Global Navigation Satellite System and six ground-based measurements. Both the model and data showed a decrease in ionospheric densities during the eclipse and an enhancement above what would happen without the eclipse after the passage of the moon. The analysis showed that the posteclipse enhancement in the ionosphere was caused by the enhanced neutral Oxygen density, which was driven by the horizontal winds, as well as decreased neutral N_2 density, which was driven primarily by the cooling of the atmosphere.

1. Introduction

Numerous studies have been conducted to investigate the electron density (Ne), electron (Te) and ion (Ti) temperatures, gravity waves, irregularities, electric fields, etc. during solar eclipse events (e.g., Chimonas & Hines, 1970; Jakowski et al., 2008; Rishbeth, 1968). The locally direct ionospheric response includes the decrease of the electron and ion temperatures due to lack of the extreme ultraviolet (EUV) heating, as well as the depletion of the electron densities resulting from the reduction of the photoionization. Studies have shown that the density below the *F* layer decreases substantially, while the net ionization in the *F* layer may decrease slightly, remain unchanged, or even increase during the solar eclipse, depending on the competing effects of the loss in photoionization and the diffusion above the F2 peak (e.g., Boitman et al., 1999; Chen et al., 2015; Ding et al., 2010; Le et al., 2009). Neutral composition and neural winds also play a crucial role in the ionospheric response to the eclipse (Le et al., 2008; Madhav et al., 2012; Müller-Wodarg et al., 1998; St.-Maurice et al., 2011, etc.).

A solar eclipse provides a good opportunity to test thermosphere-ionosphere models' response to the impulse variations of solar EUV over a limited region of the Earth, and the models can help to understand the unclear phenomena and mechanisms during the events. However, while an extensively large number of observational studies have been conducted to investigate the ionospheric response to solar eclipses, there are only a few modeling studies (Roble et al., 1986; Salah et al., 1986, etc.). Earlier simulations that lacked realistic boundary conditions, eclipse function, etc. did not match observations well and therefore needed improving (Korenkov, Klimenko, Baran, et al., 2003; Korenkov, Klimenko, Bessarab, et al., 2003; Müller-Wodarg et al., 1998, etc.). The Theoretical Ionospheric Model of the Earth in Institute of the Geology and Geophysics, Chinese Academy of Sciences, was used to simulate the midlatitude ionospheric response to solar eclipses over South and East Asia. It was found that due to the large plasma flux from the topside ionosphere, the total electron content (TEC) response around 30°N was mainly due to the electron density response below 200 km (Le et al., 2010). Pitout et al. (2013) reproduced common features of the ionospheric response to a high-latitude eclipse over EISCAT Svalbard Radars with the 1-D TRANSCAR model that describes the dynamics of different ionospheric species along a magnetic field line. Huba and Drob (2017) applied SAMI3, a global ionosphere and plasmasphere model, to predict the ionospheric response to the 21 August 2017 solar eclipse quantitatively. It was indicated that the electron density decreased by 50% in the *F* region with O^+ velocities changing from 40 m/s upward to 20 m/s downward.

The enhancement associated with the solar eclipse has been reported by both observational and simulational studies, but most of them were during the eclipse, especially during the first phase (e.g., Anastassiades & Moraitis, 1968; Cheng et al., 1992; Evans, 1965a). The during-eclipse enhancement is thought to result from the downward diffusion of ions due to the lowering of equilibrium scale height caused by a large drop in Te + Ti in the *F* region (Boitman et al., 1999; Evans, 1965b). Compared to the enhancement during the eclipse, posteclipse enhancement is rare and the physical processes are not clear. Chen et al. (2013) reported a posteclipse enhancement due to downward transport from the plasmasphere after analyzing electron profiles at middle latitudes. Huang et al. (1999) suggested that the posteclipse enhancement in TEC was due to the daily variations of the equatorial ionization anomaly (EIA) at low latitudes, while Tsai and Liu (1999) theorized that the solar eclipse induced a strengthened prereversal enhancement resulting in the posteclipse enhancement. Simulations with the Coupled Thermosphere-Ionosphere-Plasmasphere Model indicated that the enhanced [O]/[N_2] ratio contributed to the electron density enhancement after the eclipse, and Korenkov, Klimenko, Bessarab, et al. (2003) suggested that the decrease of N_2 due to cooling was the driver of the enhancement of the F2 layer critical frequency (foF2).

In this letter, we present simulation results of the Global Ionosphere-Thermosphere Model (GITM), as well as the observations from Global Positioning System (GPS) receivers and six ionosondes (see Figure 3) distributed in North and South America. The simulated response of TEC and NmF2 was consistent with observations, especially an enhancement after the eclipse which was not reproduced by Huba and Drob (2017), who made the simplifying assumption that neutral thermospheric feedback effects were negligible. Detail analysis showed that the divergence of the horizontal winds caused drove the increase in Oxygen after the eclipse allowing an increase in the ionization rate. The slower charge exchange due to both the decreased ion temperature and N_2 density allowed an increase of O^+ density in the *F* region also.

2. Methodology

The GITM is a 3-D first-principles model, which allows different models of high-latitude electric fields, auroral particle precipitation, solar EUV inputs, and particle energy deposition to be used (Ridley et al., 2006). During a solar eclipse, the Moon obscures the disk of the Sun and thus the solar EUV input into the upper atmosphere decreases in the limited region around the totality. In order to determine the path and mask for the eclipse, the coordinates of the GITM grid (X, Y, and Z) were converted into the GSE (Geocentric Solar Ecliptic) system (X_{GSE}, Y_{GSE}, and Z_{GSE}), based on the local time, latitude, and solar declination angles. It was assumed that the Moon casts a circular shadow in the (Y_{GSE}, Z_{GSE}) coordinates, while the X_{GSE} of the grid points was assumed to be much smaller than the Earth-Moon distance, such that the size of the occulted region was constant. Figures 1a and 1b show the linear path of the center of the totality region in the GSE and Geographic coordinate systems and the path from a National Aeronautics and Space Administration (NASA) website (https://informal.jpl.nasa.gov/museum/sites/default/files/ResourceLibrary/2017_eclipse_path.kml). The NASA points do not make a perfectly straight line in GSE coordinates, while here it is approximated as one. The root-mean-square difference between the linear approximation and the NASA points is 14.7 km, which is significantly smaller than the grid cells in GITM. The occultation within GITM was calculated using the distance between the GITM grid point and the center of the totality in the (Y_{GSE}, Z_{GSE}) plane. Figure 1c shows the percentage of the nominal EUV heating and ionization that occurred in the GITM cells as a function of distance away from the center point of the eclipse. It was assumed within GITM that the region of the mask has two stages: near the edge, the brightness decreased exponentially, while near the center, the brightness decreased linearly.

To validate the simulation results of the ionosphere, the global TEC and the NmF2 data from six ionosondes were analyzed. The TEC data were provided by the International Global Navigation Satellite System (GNSS) Service Ionosphere Working Group with 15-min time resolution (https://cdaweb.sci.gsfc.nasa.gov/index.

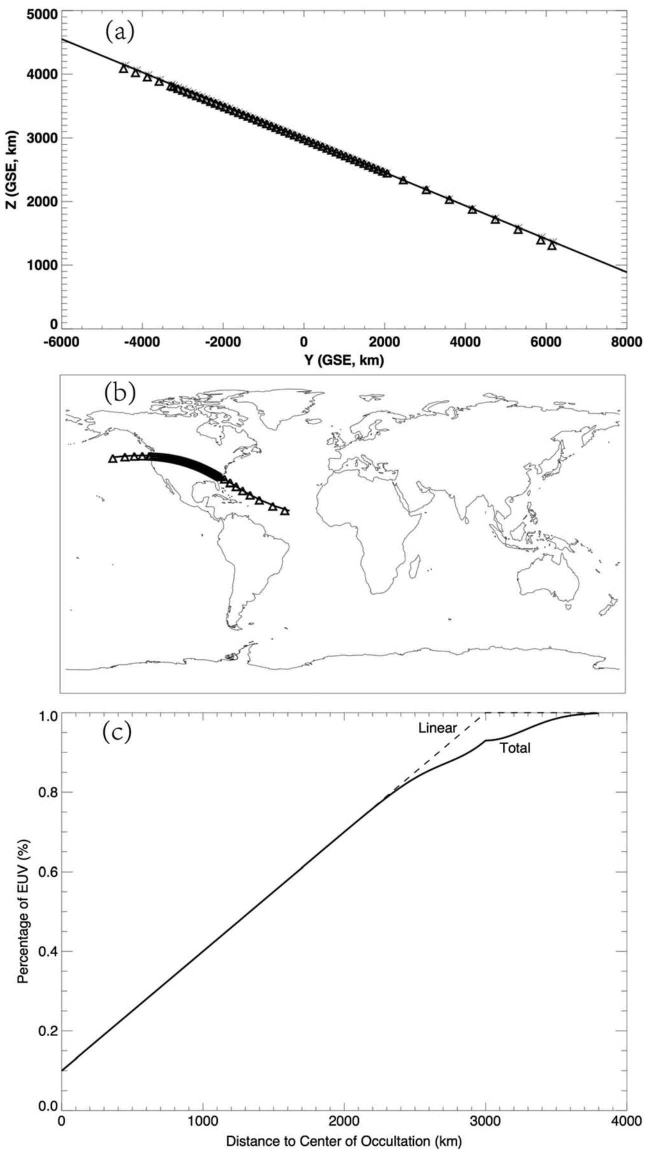

Figure 1. The path of the center of totality in Geocentric Solar Ecliptic (GSE; a) and geographic coordinates (b). The solid lines indicate the linear path as described here; the triangles indicate the National Aeronautics and Space Administration-specified locations of the totality. The stars in (a) indicate the linear path at the same time as the triangles. The percentage of the total extreme ultraviolet (EUV) heating and ionization in Global Ionosphere-Thermosphere Model as a function of distance from the center of totality (c). The solid line indicates the total percentage change; the dashed line indicates just the linear portion.

html/). The NmF2 data were derived from the ionograms provided by the Digital Ionogram Database and were manually scaled via the interactive ionogram scaling software (Reinisch et al., 2009). The time resolution of NmF2 presented in this work was 15 min in North America and 10 min in South America.

3. Results and Discussion

The lunar umbra initiated contact with North America on the west coast at approximately 16:00 UT and left the continent at approximately 20:00 UT on the east coast. Figure 2 shows the percentage differences of TEC between the eclipse and reference days (see results with more time frames in supporting information). Figure 2a shows the difference between GITM simulation results with and without the eclipse. The red line represents the path of the eclipse, and the red triangle is the umbra of the Moon at the moment that is labeled at the top of each subplot. Figure 2b is similar to Figure 2a, except it shows the GPS observations, with the baseline reference being the average of 10 quiet days ($Kp < 4$): 5 days before and 5 days after the eclipse. Both simulations and observations showed a depression during and after the eclipse. In terms of the depression during the eclipse, the temporal and spatial variations were consistent in general. The depletion began in the northwest of North America at ~17:00 UT when the totality began. The depression then expanded and propagated southeast. At ~18:30 UT, the ionosphere above almost the entire United States was depressed. This depression then shifted southeast, eventually recovering gradually after the end of the eclipse and lingering until the end of the day, although the simulated depletion disappeared more rapidly. Quantitatively, the depletion in GPS TEC was ~30–40% at 17:00 UT and reached a maximum of ~57.6% at about 18:30 UT, while the depression in the model was ~40–50% at 17:00 UT and a maximum was ~54.3% at 18:30. Coster et al. (2017) also showed difference variations of GPS TEC with 29 August 2017 as the reference day during the same eclipse event. The temporal and spatial variations of the depletion were consistent with the observational and modeling results here, though they showed a larger decrease exceeding 60%. This discrepancy might be caused by the different selection of the reference day.

Figures 3a–3d show NmF2 perturbations derived from four ionosondes in North America. The locations of the ionosondes are denoted by black triangles in the TEC maps in Figure 2. For each station, after the start of the eclipse, the simulated NmF2 began to decrease, reached the minimum after the totality of the eclipse, and then gradually recovered. The maximum reduction in each of the four locations were ~23.1%, ~40.0%, ~46.3%, and ~34.9% in GITM, and ~42.6%, ~58.3%, ~48.8%, and ~44.3% from observations. Essentially, the simulations were consistent with the observations, though the observations showed a slower recovery from the eclipse, while the GITM results showed a much more rapid recovery. The observations may also have shown a slight lag between when the totality occurred and when the minimum in NmF2 occurred, while GITM did not indicate an obvious lag. Just after the end of the eclipse, the NmF2 was still lower than the background at all the stations, although several hours later at three of the stations, the NmF2 became higher than the average.

Figures 3e and 3f show comparisons between the simulation and observations at two stations in South America. The observational NmF2 was enhanced well before the eclipse and revealed an increase during, as well as after the eclipse, while the simulated NmF2 showed little change, although extremely minor

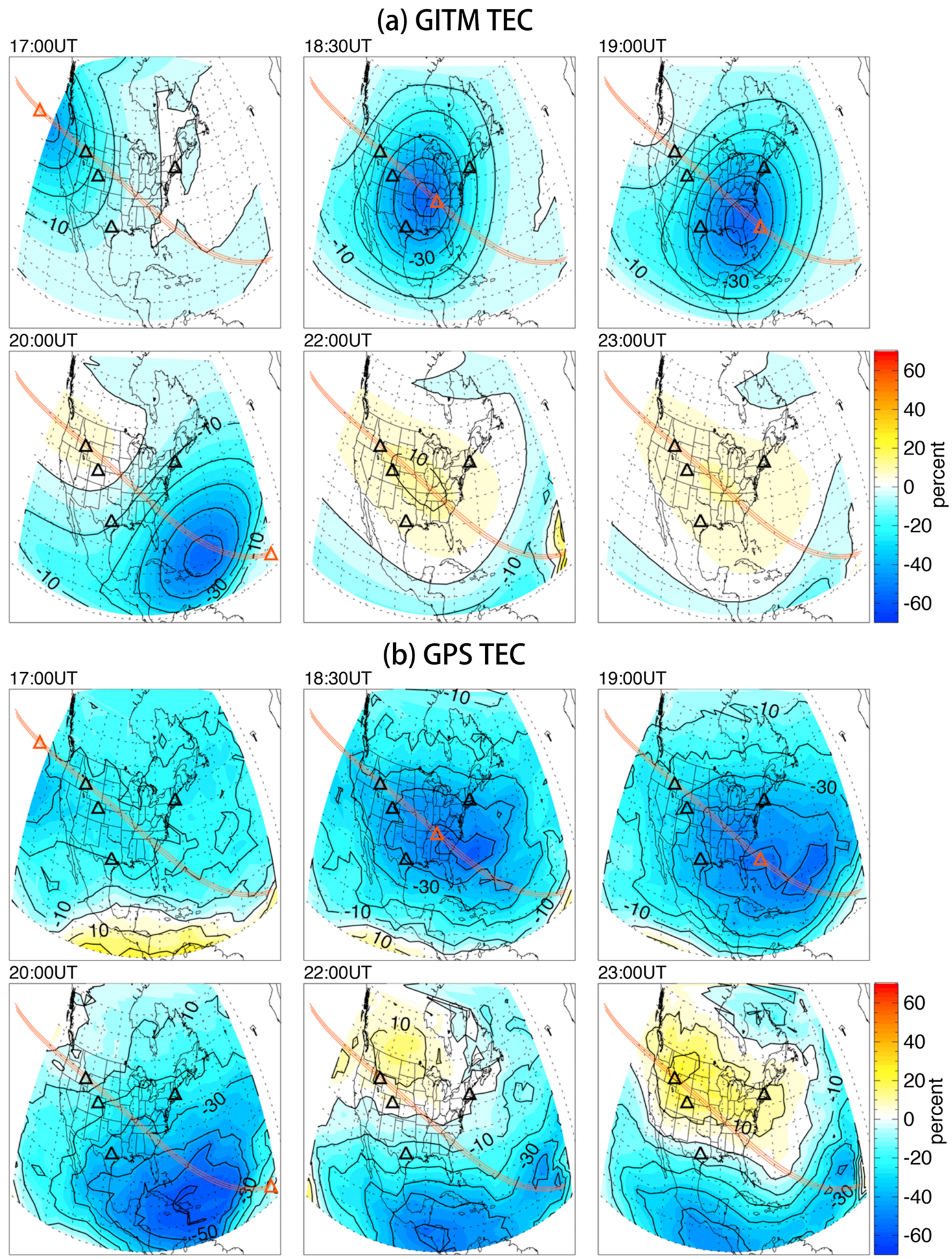

Figure 2. Percentage difference of total electron content (TEC) from Global Ionosphere-Thermosphere Model (GITM; a) and Global Positioning System (GPS; b) with the solar eclipse path (red solid line) and the totality at the moment (red triangle).

differences occurred after about 19 UT. Since the umbra of the Moon did not reach South America, it is difficult to say whether these observed variations were associated with the eclipse.

GITM predicted a posteclipse enhancement in North America associated with the solar eclipse with TEC and NmF2 increased by ~10%. In Figure 2a, the TEC enhancement began in the west at approximately 19:30 UT (not shown here) and then spread southeast along the totality path of the eclipse. About 2 hr later, the enhancement overcast the entire United States. Accordingly, in Figures 3a–3d, GITM showed enhanced NmF2 at all of the four locations after the eclipse. In Boulder (40°N, 254.7°E) and Idaho (43.8°N, 247.3°E) which were closer to the totality of the eclipse, NmF2 was increased by ~10%, while in Austin (30.4°N, 262.3°E) and Millstone Hill (42.6°N, 288.5°E) which were relatively far from the totality, NmF2 was increased less than 10%.

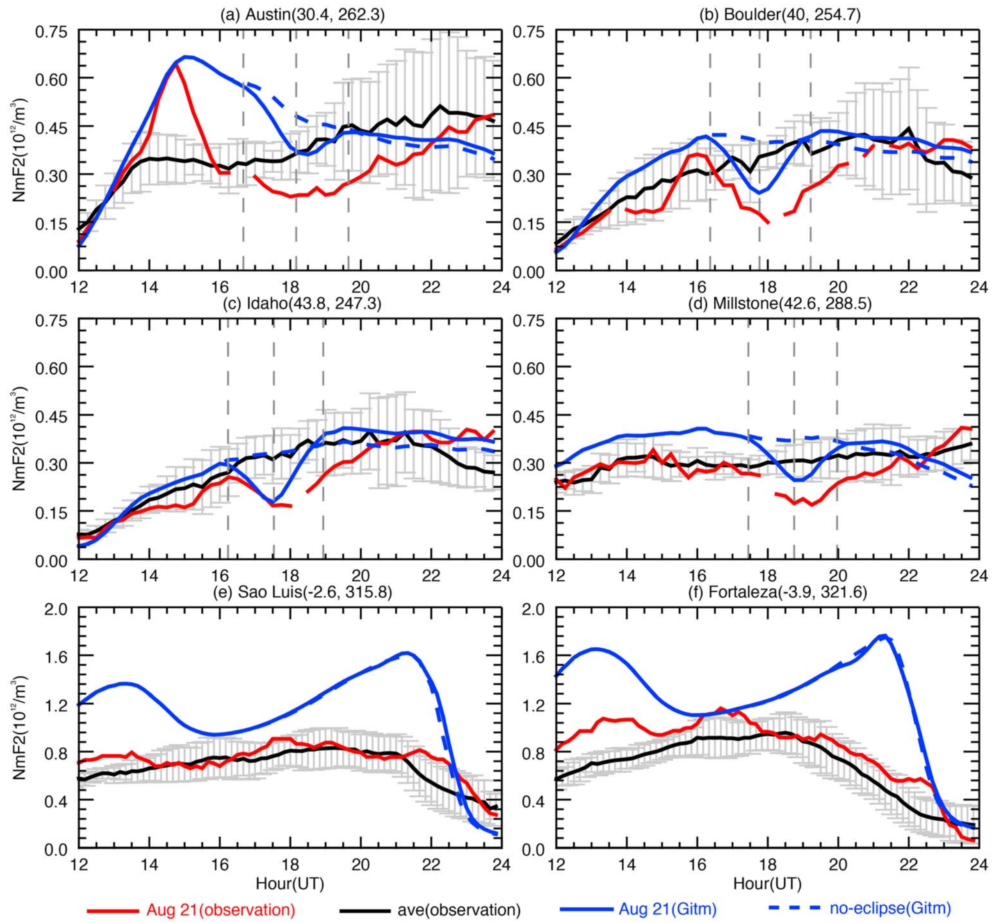

Figure 3. NmF2 in Global Ionosphere-Thermosphere Model (GITM) with (blue solid line) and without (blue dashed line) eclipse and in measurements on 21 August (red line) and reference days (black line) as a function of UT hours in North America (a–d) and South America (e and f). The gray error bars represent 1 standard deviation. The three dashed gray lines are the start, the max obscuration, and the end of the total eclipse, respectively.

This enhancement agreed relatively well with the measurements. In Figure 2b, from 21:00 UT to 23:00 UT, the GPS TEC was enhanced by ~10–25% in the United States. The enhancement also started from the west of the continent and then evolved along the totality path until it covered the entire region that was depressed during the main phase of the eclipse. In Figures 3a–3d, the NmF2 was increased up to ~30–40% in Boulder and Idaho and ~10% in Millstone Hill after approximately 22:00 UT. And Austin did not show a clear increase in NmF2 after the solar eclipse. Though all geomagnetic effects cannot be excluded in the observations, based on the comparisons with model and associations with the totality path, it appears likely that the enhancement recorded by the measurements was caused by the eclipse. Note that the variance was very large at 22 UT, indicating that the reference days may not have been very quiet.

The continuity equation of ions may help to determine what caused the density increase and can be written as follows (Schunk & Nagy, 2000):

$$\frac{\partial N_i}{\partial t} + \nabla \cdot (N_i V_i) = S - L \tag{1}$$

where N_i is the number density of the ions, V_i is the velocity of ions, S is the production rate, and L is the loss rate. The source of the enhancement could be due to advection, changes in production, or recombination processes. Evans (1965b) investigated six ionosondes distributed in Alaska, Canada, and North America revealing an enhancement of foF2 during the first phase of the eclipse. He suggested that the downward diffusion of ions resulted in the increase of electron density. Chen et al. (2013) used measurements from a network of ionosondes showing an enhancement after the solar eclipse on 15 January 2010. The electron density profiles indicated that a downward plasma flux from the plasmasphere was the driver. At low latitudes, the variations of the electron density may have been associated with the prereversal enhancements lifting the ionosphere from below (Tsai & Liu, 1999). Müller-Wodarg et al. (1998) suggested that an electron density enhancement after an eclipse was related to the neutral composition (enhanced [O]/[N_2] ratio) with the Coupled Thermosphere-Ionosphere-Plasmasphere Model. Korenkov, Klimenko, Bessarab, et al. (2003) modeled the 11 August 1999 solar eclipse and compared foF2 with experimental data. An enhanced foF2 after the eclipse could be discerned, which was suggested to be driven by a decrease of N_2 due to cooling.

GITM is not coupled with a plasmasphere, and Huba and Drob (2017) did not reproduce the posteclipse enhancement with the ionosphere-plasmasphere model; therefore, the downward diffusion of ions is most likely not the source during this particular eclipse, even though there was a strong change in Te. Also, the enhanced region was too far away from the EIA to be affected by the electrojets. Figures 4a–4g show simulated variations of neutral temperature, ion temperature, neutral vertical wind, zonal wind, meridional wind, N_2 density, and O density at 300 km in Idaho (43.8°N, 247.3°E). At the onset of the eclipse, the neutral temperature, as well as the ion and electron (not shown) temperatures, decreased dramatically. The upward vertical neutral wind reversed direction due to the lowering of pressure, while both the westward and northward winds increased after the totality. The downwelling of the pressure level decreased the neutral density at a fixed altitude (Müller-Wodarg et al., 1998), although the individual species variation differed due to the different gradients involved. After the maximum obscuration, the neutral temperature started to recover and the atmosphere began to expand. Simultaneously, the O and N_2 densities started to increase toward the noneclipse state; however, the O density was enhanced above the noneclipse case after and even before the end of the eclipse, while the N_2 density was still lower than the expected value after the eclipse, driving an increased [O]/[N_2] ratio. In the *F* region, the O^+ ions are mainly produced by the ionization of O, and lost due to charge exchange with N_2. The increase of the [O]/[N_2] ratio therefore was likely to be the source of the enhanced electron density after the eclipse.

The different dynamics of O and N_2 are puzzling. The vertical continuity equation for each species is

$$\frac{\partial N_n}{\partial t} = -N_n \nabla \cdot \mathrm{V}_n - \mathrm{V}_n \cdot \frac{\partial N_n}{\partial r} \tag{2}$$

where N_n and V_n are the number density and the vertical velocity of the neutral species, respectively, $-N_n\nabla \cdot \mathrm{V}_n$ is the divergence term, and $-\mathrm{V}_n \cdot \frac{\partial N_n}{\partial r}$ is the advection term. The total of the divergence term and advection term determines the change of density. Based on equation (2), the rate of change of O and N_2 density was calculated in both vertical and horizontal directions. The integral of the rate of change caused by the different terms was also calculated. Figures 4h–4j show the density differences caused by different terms for O and N_2 between runs with and without the eclipse as a function of time at 300 km in Idaho (43.8°N, 247.3°E). In the vertical direction (blue lines), the divergence term (Figure 4h) contributed a slight increase of O and N_2, while the advection term (Figure 4i) drove a substantial decrease in the density. Therefore, in the vertical direction (blue lines), the total for O and N_2 (Figure 4j) was decreased by ~$0.8 \times 10^{14}/\mathrm{m}^3$ and ~$0.4 \times 10^{14}/\mathrm{m}^3$ during the eclipse and started to recover before the end of the eclipse. Consequently, if only the vertical direction was considered, both the O and N_2 densities would have decreased though out the eclipse, taking several hours to recover. In the horizontal direction (red lines), the divergence term (Figure 4h) was dominated for both O and N_2, while the advection term (Figure 4i) was quite small. These two terms together (Figure 4j) resulted in an increase of O by ~$0.9 \times 10^{14}/\mathrm{m}^3$ and N_2 by ~$0.3 \times 10^{14}/\mathrm{m}^3$ after the beginning of the solar eclipse. The sum of the total in the vertical and horizontal direction showed that the O and N_2 decreased at the onset of the eclipse and then started to recover after the totality. However, the O was enhanced before the end of the eclipse, while N_2 remained lower than the noneclipse state. For O, the minimum of the depression was ~$-0.3 \times 10^{14}/\mathrm{m}^3$ while the maximum was ~$0.2 \times 10^{14}/\mathrm{m}^3$. The divergence in the horizontal wind caused the increase in Oxygen after the eclipse. When the eclipse started, the decrease of the temperature caused the decrease in the pressure, resulting in the contraction of the atmosphere and the convergence of winds. The downward winds led the decrease of the density. As the horizontal winds accelerated away from their nominal behavior, a convergence in the winds started to develop. Because the density of O was much larger than the density of N_2, the horizontal convergence term in O became larger than vertical downwelling, resulting in a net increase in O, while N_2 continued to be lower than nominal conditions.

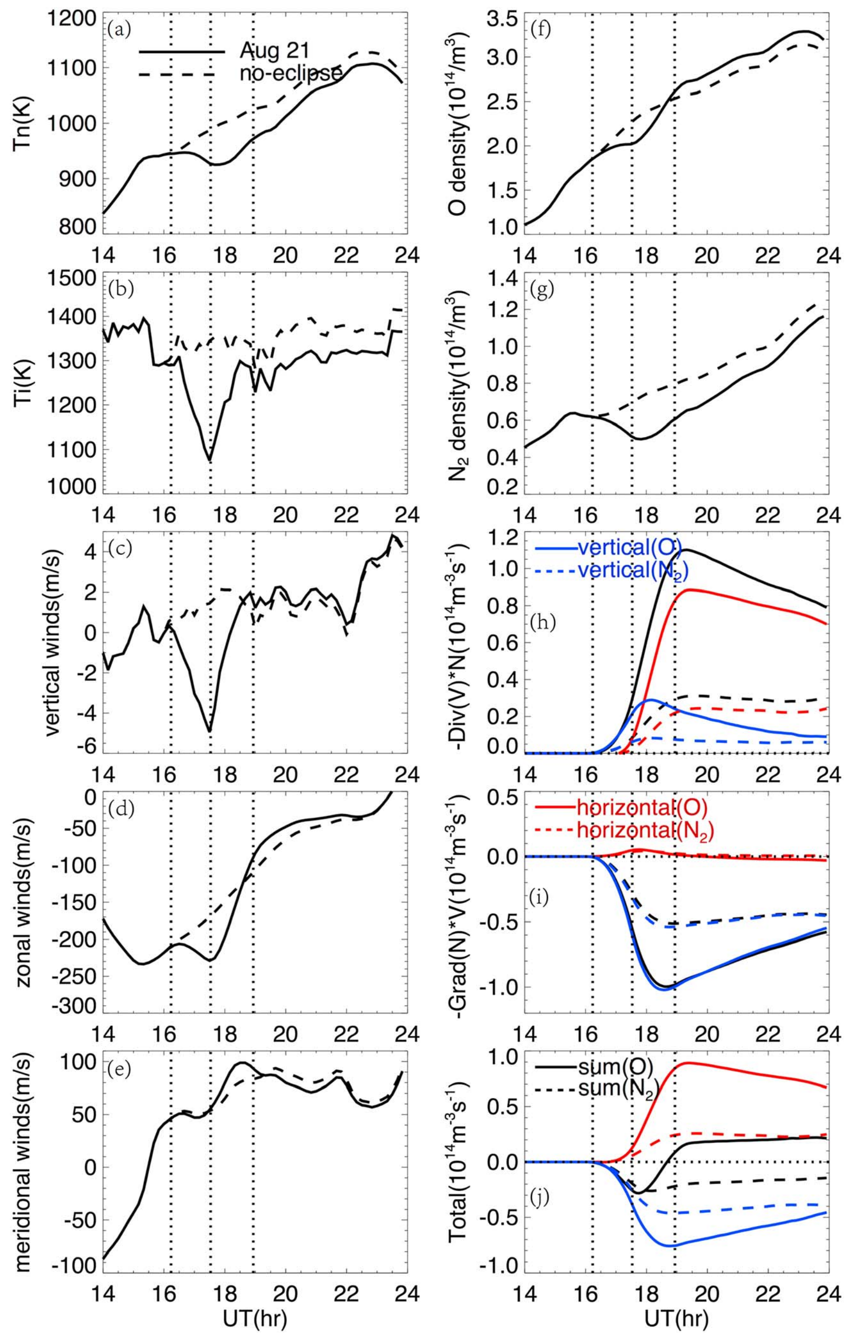

Figure 4. Simulated neutral temperature (a), ion temperature (b), neutral vertical wind (c), zonal wind (d), meridional wind (e), N_2 density (f), and O density (g) with (solid line) and without eclipse (dashed line) as a function of UT hours; density difference of O (solid lines) and N_2 (dashed lines) between runs with and without eclipse as a function of UT hours derived from the divergence term (h), advection term (i) and total (j) in the continuity equation for the vertical (blue lines), horizontal direction (red lines) and total of the two directions (black lines).

In addition to the enhanced O density, the ion temperature (Figure 4b) and the N_2 density (Figure 4g) were decreased both during and after the eclipse. Both the ion temperature and the N_2 density play a strong role in the charge exchange rate between O^+ and N_2, the main loss mechanism in the F_2 ionosphere. The decreased ion temperature reduced the charge exchange rate constant (Torr & Torr, 1978), while the decreased N_2 would have directly reduced the loss rate, which may have contributed to the enhanced electron density after the eclipse.

4. Conclusions

We have simulated the total solar eclipse of 21 August 2017 with the GITM and compared the results with GPS TEC, as well as NmF2 derived from six ionosondes. The conclusions we have made from the simulation and data-model comparisons are the following:

1. A direct decrease of TEC was revealed by both the model and measurements with consistent temporal and spatial variations. The TEC was reduced by ~54.3% in the model and ~57.6% in measurements, while the NmF_2 was decreased by ~20–50% in the model and ~40–60% in measurements. After the eclipse, the depression shifted southeast recovering gradually and lingered until the end of the day.
2. A posteclipse enhancement that was not reproduced by SAMI3, which ignored neutral thermospheric feedback effects, was discerned after ~21:00 UT over the United States where the TEC increased by ~10% in GITM and ~10–25% in the measurements, and NmF2 increased by ~10% in GITM and ~10–40% in the measurements which is likely to be caused by enhanced [O]/[N_2] ratio due to different dynamics of O and N_2, as well as decreased ion temperature.
3. Detail analysis of the terms in the continuity equation indicated that the divergence in the horizontal wind drove the increase in Oxygen after the eclipse allowing an increase in the ionization rate. The slower charge exchange caused by both the decreased ion temperature and N_2 density allowed an increase of O^+ density in the *F* region also.

Acknowledgments
The NOAA Space Weather Prediction Center provided the interplanetary magnetic field data and solar wind data of the NASA Advanced Composition Explorer (ACE) satellite, as well as the F10.7 index. This paper also used ionospheric data from the Digisonde network, TEC data from the International Global Navigation Satellite Systems (GNSS) Service Ionosphere Working Group. Model results and input files, and GITM code are available upon request, while the GITM code is available on GitHub. One of the test cases contains the parameters to set up the eclipse simulation. This research was supported by AFOSR under DDDAS (Dynamic Data-Driven Applications Systems http://www.1dddas.org/) grant FA9550-16-1-0071 and partially funded by NASA NNX14E046 and NSF 1452097. L. Goncharenko was partially supported by NASA grant NNX17AH71G. We thank Douglas Drob for his helpful discussion and providing example files of the EUV mask, allowing the creation of the geometric mask used within the study.

References

Anastassiades, M., & Moraitis, G. (1968). On the behavior of *fo*F2 during the 20 May 1966 solar eclipse. *Journal of Atmospheric and Terrestrial Physics*, *30*(8), 1471–1478. https://doi.org/10.1016/S0021-9169(68)90191-8

Boitman, O. N., Kalikhman, A. D., & Tashchilin, A. V. (1999). The midlatitude ionosphere during the total solar eclipse of March 9, 1997. *Journal of Geophysical Research*, *104*(A12), 28,197–28,206. https://doi.org/10.1029/1999JA900228

Chen, G., Qi, H., Ning, B., Zhao, Z., Yao, M., Deng, Z., et al. (2013). Nighttime ionospheric enhancements induced by the occurrence of an evening solar eclipse. *Journal of Geophysical Research: Space Physics*, *118*, 6588–6596. https://doi.org/10.1002/jgra.50551

Chen, G., Wu, C., Huang, X., Zhao, Z., Zhong, D., Qi, H., et al. (2015). Plasma flux and gravity waves in the midlatitude ionosphere during the solar eclipse of 20 May 2012. *Journal of Geophysical Research: Space Physics*, *120*, 3009–3020. https://doi.org/10.1002/2014JA020849

Cheng, K., Huang, Y.-N., & Chen, S.-W. (1992). Ionospheric effects of the solar eclipse of September 23, 1987, around the equatorial anomaly crest region. *Journal of Geophysical Research*, *97*(A1), 103–111. https://doi.org/10.1029/91JA02409

Chimonas, G., & Hines, C. O. (1970). Atmospheric gravity waves induced by a solar eclipse. *Journal of Geophysical Research*, *75*(4), 875–875. https://doi.org/10.1029/JA075i004p00875

Coster, A. J., Goncharenko, L., Zhang, S.-R., Erickson, P. J., Rideout, W., & Vierinen, J. (2017). GNSS observations of ionospheric variations during the 21 August 2017 solar eclipse. *Geophysical Research Letters*, *44*, 12,041–12,048. https://doi.org/10.1002/2017GL075774

Ding, F., Wan, W., Ning, B., Liu, L., le, H., Xu, G., et al. (2010). GPS TEC response to the 22 July 2009 total solar eclipse in East Asia. *Journal of Geophysical Research*, *115*, A07308. https://doi.org/10.1029/2009JA015113

Evans, J. V. (1965a). An *F* region eclipse. *Journal of Geophysical Research*, *70*(1), 131–142. https://doi.org/10.1029/JZ070i001p00131

Evans, J. V. (1965b). On the behavior of *fo*F2 during solar eclipses. *Journal of Geophysical Research*, *70*(3), 733–738. https://doi.org/10.1029/JZ070i003p00733

Huang, C. R., Liu, C. H., Yeh, K. C., Lin, K. H., Tsai, W. H., Yeh, H. C., & Liu, J. Y. (1999). A study of tomographically reconstructed ionospheric images during a solar eclipse. *Journal of Geophysical Research*, *104*(A1), 79–94. https://doi.org/10.1029/98JA02531

Huba, J. D., & Drob, D. (2017). SAMI3 prediction of the impact of the 21 August 2017 total solar eclipse on the ionosphere/plasmasphere system. *Geophysical Research Letters*, *44*, 5928–5935. https://doi.org/10.1002/2017GL073549

Jakowski, N., Stankov, S. M., Wilken, V., Borries, C., Altadill, D., Chum, J., et al. (2008). Ionospheric behavior over Europe during the solar eclipse of 3 October 2005. *Journal of Atmospheric and Solar-Terrestrial Physics*, *70*(6), 836–853. https://doi.org/10.1016/j.jastp.2007.02.016

Korenkov, Y. N., Klimenko, V. V., Baran, V., Shagimuratov, I. I., & Bessarab, F. S. (2003). Model calculations of TEC over Europe during 11 August 1999 solar eclipse. *Advances in Space Research*, *31*(4), 983–988. https://doi.org/10.1016/S0273-1177(02)00815-3

Korenkov, Y. N., Klimenko, V. V., Bessarab, F. S., Nutsvalyan, N. S., & Stanislawska, I. (2003). Model/data comparison of the *F*2-region parameters for the 11 August 1999 solar eclipse. *Advances in Space Research*, *31*(4), 995–1000. https://doi.org/10.1016/S0273-1177(02)00816-5

Le, H., Liu, L., Ding, F., Ren, Z., Chen, Y., Wan, W., et al. (2010). Observations and modeling of the ionospheric behaviors over the East Asia zone during the 22 July 2009 solar eclipse. *Journal of Geophysical Research*, *115*(A10), A10313. https://doi.org/10.1029/2010JA015609

Le, H., Liu, L., Yue, X., & Wan, W. (2008). The midlatitude F2 layer during solar eclipses: Observations and modeling. *Journal of Geophysical Research*, *113*(A8), A08309. https://doi.org/10.1029/2007JA013012

Le, H., Liu, L., Yue, X., Wan, W., & Ning, B. (2009). Latitudinal dependence of the ionospheric response to solar eclipses. *Journal of Geophysical Research*, *114*(A7), A07308. https://doi.org/10.1029/2009JA014072

Madhav Haridas, M. K., & Manju, G. (2012). On the response of the ionospheric *F* region over Indian low-latitude station Gadanki to the annular solar eclipse of 15 January 2010. *Journal of Geophysical Research*, *117*, A01302. https://doi.org/10.1029/2011JA016695

Müller-Wodarg, I. C. F., Aylward, A. D., & Lockwood, M. (1998). Effects of a mid-latitude solar eclipse on the thermosphere and ionosphere—A modelling study. *Geophysical Research Letters*, *25*(20), 3787–3790. https://doi.org/10.1029/1998GL900045

Pitout, F., Blelly, P.-L., & Alcaydé, D. (2013). High-latitude ionospheric response to the solar eclipse of 1 August 2008: EISCAT observations and TRANSCAR simulation. *Journal of Atmospheric and Terrestrial Physics*, *105-106*, 336–349. https://doi.org/10.1016/j.jastp.2013.02.004

Reinisch, B. W., Galkin, I. A., Khmyrov, G. M., Kozlov, A. V., Bibl, K., Lisysyan, I. A., et al. (2009). New Digisonde for research and monitoring applications. *Radio Science*, *44*, RS0A24. https://doi.org/10.1029/2008RS004115

Ridley, A., Deng, Y., & Tòth, G. (2006). The global ionosphere-thermosphere model. *Journal of Atmospheric and Solar: Terrestrial Physics*, *68*(8), 839–864. https://doi.org/10.1016/j.jastp.2006.01.008

Rishbeth, H. (1968). Solar eclipses and ionospheric theory. *Space Science Reviews*, *8*, 543–554.

Roble, R. G., Emery, B. A., & Ridley, E. C. (1986). Ionospheric and thermospheric response over Millstone Hill to the May 30, 1984, annular solar eclipse. *Journal of Geophysical Research*, *91*(A2), 1661–1670. https://doi.org/10.1029/JA091iA02p01661

Salah, J. E., Oliver, W. L., Foster, J. C., Holt, J. M., Emery, B. A., & Roble, R. G. (1986). Observations of the May 30, 1984, annular solar eclipse at Millstone Hill. *Journal of Geophysical Research*, *91*(A2), 1651–1660. https://doi.org/10.1029/JA091iA02p01651

Schunk, W. R., & Nagy, A. F. (2000). *Ionospheres: Physics, plasma physics, and chemistry* (pp. 606–607). Cambridge, UK: Cambridge University Press. https://doi.org/10.1017/CBO9780511551772

St.-Maurice, J.-P., Ambili, K. M., & Choudhary, R. K. (2011). Local electrodynamics of a solar eclipse at the magnetic equator in the early afternoon hours. *Geophysical Research Letters*, *38*, L04102. https://doi.org/10.1029/2010GL046085

Torr, D. G., & Torr, M. R. (1978). Review of rate coefficients of ionic reactions determined from measurements made by the Atmosphere Explorer satellites. *Reviews of Geophysics*, *16*(3), 327–340. https://doi.org/10.1029/RG016i003p00327

Tsai, H. F., & Liu, J. Y. (1999). Ionospheric total electron content response to solar eclipses. *Journal of Geophysical Research*, *104*(A6), 12,657–12,668. https://doi.org/10.1029/1999JA900001